ARTICLES
https://doi.org/10.1038/s41929-018-0134-1
nature catalysis

Overall water splitting by Ta_3N_5 nanorod single crystals grown on the edges of $KTaO_3$ particles

Zheng Wang[1,5], Yasunobu Inoue[1,2], Takashi Hisatomi[1,5], Ryo Ishikawa[3], Qian Wang[1], Tsuyoshi Takata[1,5], Shanshan Chen[1,5], Naoya Shibata[3], Yuichi Ikuhara[3] and Kazunari Domen[1,4*]

Although one-step-excitation overall water splitting on a particulate photocatalyst is a simple means of performing scalable solar-to-hydrogen energy conversion, there is a lack of photocatalysts with significant activity under visible light. Despite its superior visible-light absorption, the Ta_3N_5 photocatalyst has not accomplished overall water splitting due to strong charge recombination at defects. Here, we show rapid growth of Ta_3N_5 nanorods on lattice-matched cubic $KTaO_3$ particles through the volatilization of potassium species during a brief nitridation process. The Ta_3N_5 nanorods generated selectively on the edge of $KTaO_3$ are spatially separated and well-defined single crystals free from grain boundaries. When combined with the Rh/Cr_2O_3 co-catalyst, the single-crystal Ta_3N_5 nanorods split water into hydrogen and oxygen very efficiently under visible light and simulated sunlight. Our findings demonstrate the importance of nanostructured single-crystal photocatalysts free from structural defects in solar water splitting.

In view of constantly increasing global energy demands and related environmental issues, the pursuit of renewable and ecofriendly energy sources has become extremely important[1,2]. As such, the utilization of inexhaustible solar energy to generate clean, storable hydrogen from water using photocatalytic and/or photoelectrochemical processes has been intensively investigated[3–7]. Extremely high solar-to-hydrogen (STH) conversion efficiencies have been demonstrated at the laboratory scale based on customized tandem photoelectrodes[6,7]. However, techno-economical analyses have pointed out that prohibitively high capital cost prevents photoelectrochemical devices from being implemented for solar hydrogen production process at the commercial scale[8,9]. In this scenario, the direct decomposition of water into H_2 and O_2 on particulate photocatalysts via one-step excitation is believed to be a simple and cost-effective alternative towards applicable hydrogen production on a large scale[8–12]. A particulate photocatalyst-based panel reactor has been shown to maintain the intrinsic water-splitting activity of photocatalysts regardless of size, and to be readily extensible to the level of square metres or larger[12]. Moreover, very recent drastic improvement in the apparent quantum efficiency (AQE) for one-step-excitation overall water splitting in the near-ultraviolet region (to 69% at 365 nm) demonstrates substantial potential for particulate photocatalysis[13]. Thus, the development of efficient overall-water-splitting particulate photocatalysts is a core issue. Powdered photocatalysts that function under ultraviolet irradiation have been found among metal oxides[14], and visible-light-responsive photocatalysts, which are essential for the efficient utilization of the solar spectrum, have been identified within the (oxy)nitrides family[10,11,15], cation-doped oxides[16] and plasmonic photocatalysts[17]. However, there are still only a small number of visible-light-driven photocatalysts capable of decomposing water into hydrogen and oxygen via one-step excitation with an acceptable STH energy conversion efficiency.

Owing to its simple chemical composition and narrow band gap energy of 2.1 eV, Ta_3N_5 has been regarded as a promising candidate for solar hydrogen production. This material was first reported to have a band position suitable for H^+ reduction and H_2O oxidation in 2002, and was found to photocatalytically evolve H_2 and O_2 individually from aqueous solutions containing sacrificial reagents[18]. Since then, various approaches have been suggested for the activation of Ta_3N_5 to allow one-step-excitation overall water splitting, including detailed examinations of NH_3 nitridation conditions, morphological control and surface modifications. In addition, there have been considerable improvements with regard to H_2 or O_2 evolution from half reactions[19–21], Z-scheme water splitting[22] and photoelectrochemical water oxidation[23–26] (see Supplementary Table 1). However, despite the tremendous effort over the past one and a half decades, overall water splitting has not yet been realized on Ta_3N_5 particulate photocatalysts owing to the strong recombination and trapping of photogenerated charges in the absence of sacrificial agents and applied voltage. Thus, the activation of Ta_3N_5 for overall water splitting remains an important challenge related to the successful utilization of long-wavelength visible light in photocatalytic water splitting.

Ta_3N_5 prepared by prolonged nitridation (10 h nitridation or longer) under an NH_3 flow at high temperatures generally consists of aggregated polycrystalline particulates incorporating grain boundaries and defects[27], which operate as recombination and trapping centres for photogenerated electron-hole pairs[14,27]. As a result, the separation of photoexcited charges and the migration of electrons and holes to surface sites for photocatalytic reactions become inefficient, and so it is desirable to obtain good-quality Ta_3N_5 single crystals[27]. $KTaO_3$ is a unique starting metal oxide for the synthesis of Ta_3N_5 because it has a lattice spacing close to that of Ta_3N_5 and contains an element (potassium) that readily vaporizes at high temperatures. Herein, we demonstrate the spontaneous growth of Ta_3N_5 nanorod single crystals on the edge sites of $KTaO_3$ cubes following a relatively short NH_3 nitridation process, without the requirement for an additional template or any special techniques.

[1]Department of Chemical System Engineering, School of Engineering, The University of Tokyo, Tokyo, Japan. [2]Japan Technological Research Association of Artificial Photosynthetic Chemical Process, Tokyo, Japan. [3]Institute of Engineering Innovation, The University of Tokyo, Tokyo, Japan. [4]Centre for Energy and Environmental Science, Shinshu University, Nagano, Japan. [5]Present address: Centre for Energy and Environmental Science, Shinshu University, Nagano, Japan. *e-mail: domen@chemsys.t.u-tokyo.ac.jp

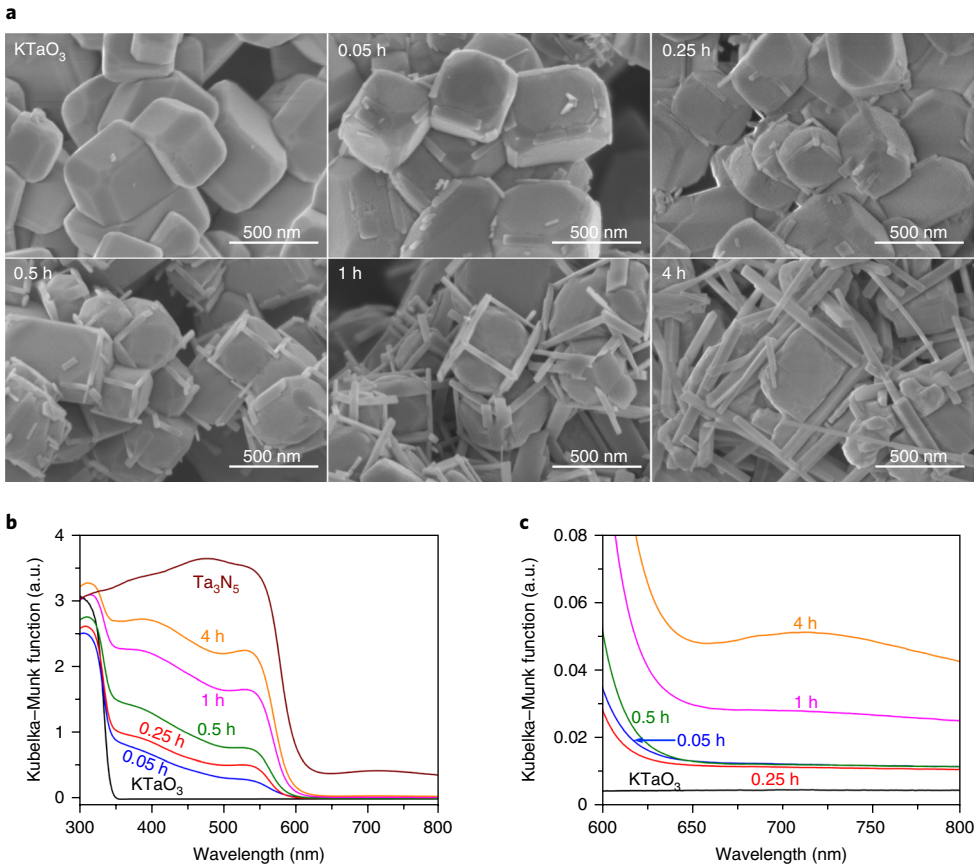

Fig. 1 | Morphology and UV-Vis DRS analysis of $Ta_3N_5/KTaO_3$. a, SEM images of $KTaO_3$, and $Ta_3N_5/KTaO_3$ synthesized with nitridation times of 0.05, 0.25, 0.5, 1 and 4 h. **b**,**c**, UV-Vis DRS acquired from $KTaO_3$, $Ta_3N_5/KTaO_3$ synthesized with nitridation times of 0.05, 0.25, 0.5, 1 and 4 h, and Ta_3N_5.

The volatilization of potassium species from the lattice-matched $KTaO_3$ surface promotes the fast evolution of Ta_3N_5 nanorod single crystals free from grain boundaries and prevents the Ta_3N_5 phase from long exposure to the reducing NH_3 atmosphere, which generates defects. These Ta_3N_5 nanorod single crystals exhibit activity for one-step-excitation overall water splitting under visible light ($\lambda \geq 420$ nm) or simulated sunlight.

Results

Characterization of Ta_3N_5 nanorod single crystals. The preparation of $KTaO_3$, its subsequent nitridation under NH_3 and the photocatalytic decomposition of water are all described in detail in the Methods. Briefly, $KTaO_3$ was synthesized by a conventional solid-state reaction in air at 1,423 K for 10 h. The prepared $KTaO_3$ was then subjected to a brief nitridation process (0.05 to 4 h) at 1,173 K under a flow of gaseous NH_3 (100 ml min^{-1}), yielding a Ta_3N_5 phase grown on the $KTaO_3$ (denoted hereafter as $Ta_3N_5/KTaO_3$).

Figure 1a presents scanning electron microscopy (SEM) images of the $KTaO_3$ and nitrided samples. Pristine $KTaO_3$ particles exhibited cuboid shapes with broad edges at the ridges. Nitridation at 1,173 K for 0.05 h resulted in only minimal changes to the flat faces of the $KTaO_3$ cubes, retaining the rectangular shape, but produced rod-like crystals at the edges of the cubes. The X-ray diffraction (XRD) pattern for this sample contains small peaks attributable to a Ta_3N_5 phase in addition to large peaks attributable to the original $KTaO_3$. No other crystal phases (such as TaON) were observed (Supplementary Fig. 1). On this basis, the nanorods generated on the $KTaO_3$ are believed to have been Ta_3N_5 crystals. These nanorods gradually increased in size as the nitridation time was increased from 0.25 to 4 h (Fig. 1a), while retaining the $KTaO_3$ phase. During this process, the spatially separated Ta_3N_5 nanorods were selectively generated on the edges of $KTaO_3$ cubes, growing predominantly along these edges. The growth of Ta_3N_5 nanorod crystals was also confirmed by the increased intensity of the XRD peaks assigned to this phase (Supplementary Fig. 1). The mass fraction of Ta_3N_5, as estimated from the relative XRD peak intensities (Supplementary Fig. 2 and Supplementary Table 2), increased from 0.7 to 5.6 wt% when the nitridation time was extended from 0.05 to 4 h.

Ultraviolet-visible diffuse reflectance spectroscopy (UV-Vis DRS) (Fig. 1b) demonstrated that the onset of light absorption for this material occurs at approximately 600 nm, which is characteristic of the photoabsorption of Ta_3N_5. At shorter wavelengths, the absorption became gradually stronger, with a small bump at approximately 540 nm similar to that produced by pure Ta_3N_5 and a very sharp peak at 350 nm due to absorption by the $KTaO_3$. With increasing nitridation time, the absorption by Ta_3N_5 increased. It is notable that the background absorption at longer wavelengths beyond 600 nm was much weaker in the case of $Ta_3N_5/KTaO_3$ than is normally observed for Ta_3N_5 powder prepared from Ta_2O_5 (Fig. 1b). This is indicative of a lower density of defects caused by the reduced Ta^{5+} species or nitrogen vacancies in the Ta_3N_5 nanocrystals prepared by the nitridation of $KTaO_3$[20,27].

To further characterize the Ta_3N_5 nanocrystals on the $KTaO_3$, the $Ta_3N_5/KTaO_3$ samples nitrided at 1,173 K for 0.25 and 4 h were examined by scanning transmission electron microscopy (STEM). As shown in Fig. 2a–d, each Ta_3N_5 nanorod is a single crystal in which a regular arrangement of atoms can be observed from the surface to the interior, without any evident dislocations or grain boundaries. Annular dark field STEM (ADF-STEM) images with atomic resolution are presented in Fig. 2f and Supplementary Fig. 3b–d,

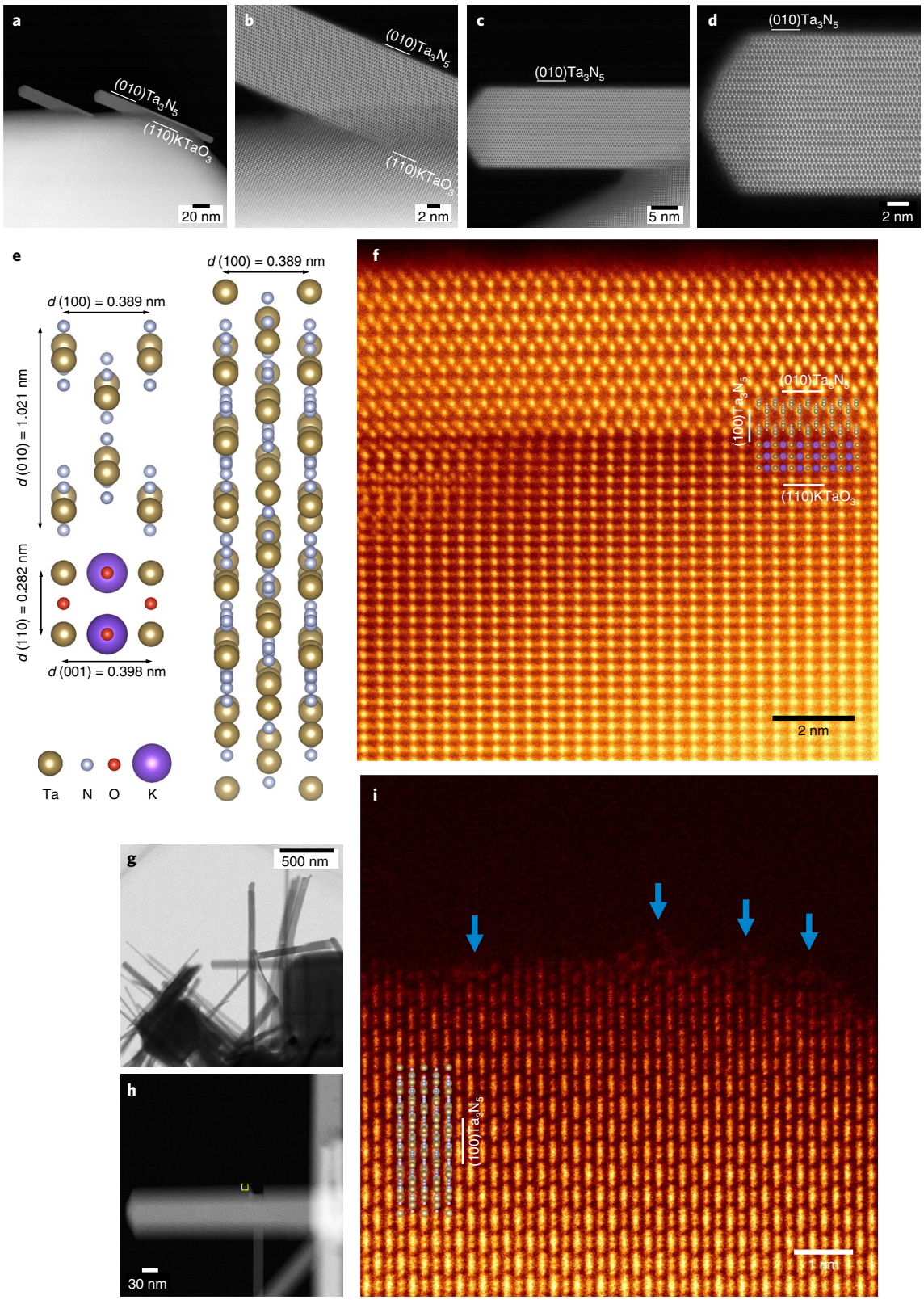

Fig. 2 | Single-crystal structure of Ta_3N_5 nanorods grown on $KTaO_3$. a–d, ADF-STEM images of $Ta_3N_5/KTaO_3$ synthesized with a nitridation time of 0.25 h, viewed from the [001] direction of the Ta_3N_5. The lines indicate the crystal facets. **e**, Crystal structures of Ta_3N_5 projected from the [001] (top left) and [041] (right) directions, and $KTaO_3$ projected from the [1–10] direction (bottom left), depicted using the Vesta programme[41]. *d* indicates the interplanar distance. **f**, Colourized and magnified ADF-STEM images of a Ta_3N_5 nanorod in $Ta_3N_5/KTaO_3$ synthesized with a nitridation time of 0.25 h viewed from the [001] direction of the Ta_3N_5. Insets: depicted crystal structures of Ta_3N_5 projected from the [001] direction and $KTaO_3$, as shown in **e**. The lines indicate the crystal facets. **g**,**h**, ADF-STEM images of $Ta_3N_5/KTaO_3$ synthesized with a nitridation time of 4 h. **i**, Colourized and magnified ADF-STEM images of a Ta_3N_5 nanorod in $Ta_3N_5/KTaO_3$ synthesized with a nitridation time of 4 h, viewed from the [041] direction of Ta_3N_5 and corresponding to the square area in **h**. Inset: depicted crystal structure of Ta_3N_5 projected from the [041] direction, as shown in **e**. The arrows and the line indicate the disordered atom arrangement at the surface and the crystal facet, respectively.

together with structural models of Ta_3N_5 and $KTaO_3$ (Fig. 2e and Supplementary Fig. 3a) that correlate the image spots with atom positions. As mentioned in Supplementary Fig. 3 and the accompanying discussion, the rapid volatilization of potassium species from the lattice-matched $KTaO_3$ (110) planes allows the Ta_3N_5 crystal phase to be initially generated on the $KTaO_3$ (110) surface, grown along the $KTaO_3$ [110] direction and elongated along the [100] orientation of the Ta_3N_5. This process forms Ta_3N_5 nanorods parallel to the edges of the $KTaO_3$ cubes (that is, the (110) planes) and explains the morphology of the Ta_3N_5 crystals in the SEM images. Notably, the characteristic Ta_3N_5 nanorods were not produced when $KTaO_3$ was nitrided in the presence of K_2CO_3 or when Ta_2O_5, $LiTaO_3$ or $NaTaO_3$ was nitrided under the same nitridation conditions (see Supplementary Figs. 4 and 5 and the accompanying discussion). Therefore, we conclude that both the close match of the lattice spacings for $KTaO_3$ and the volatilization of potassium compounds from the $KTaO_3$ are important factors promoting the spontaneous formation of Ta_3N_5 nanorod single crystals free from grain boundaries and defect states during the brief nitridation process. With the increased nitridation time to 4 h, Ta_3N_5 nanorod single crystals became larger (Fig. 2g,h) and a distorted surface atomic arrangement was clearly observed on the large-sized Ta_3N_5 nanorod single crystal (as indicated in Fig. 2i), in contrast with the smooth and regular surface of small Ta_3N_5 single crystals in Ta_3N_5/$KTaO_3$ nitrided for 0.25 h (Fig. 2a,f). This indicates that the structural defects are generated in Ta_3N_5 nanorod single crystals suffering the prolonged nitridation process, which is in agreement with the increased background absorption in the UV-Vis DRS of Ta_3N_5/$KTaO_3$ (Fig. 1c).

Overall water splitting by Ta_3N_5 nanorod single crystals. Our group has previously demonstrated that metal particles capped with Cr_2O_3 shells act as highly efficient co-catalysts that promote H_2 generation while suppressing the reverse reaction during overall water splitting[28]. In the present work, the photocatalytic activity for overall water splitting over Ta_3N_5/$KTaO_3$ was examined under visible light ($\lambda \geq 420$ nm) after the deposition of core-shell-structured M/Cr_2O_3 (M = Rh, Pt, Ir or Ru) co-catalysts. As shown in Supplementary Fig. 6, both H_2 and O_2 were produced simultaneously, along with small amounts of N_2. The little evolution of N_2 is attributed to the oxidation of unstable surface nitride species by photoexcited holes[11]. The photocatalytic activity decreased in the order of Rh > Pt > Ir > Ru. Since rhodium provided the highest activity in the present photocatalytic system, this metal was used in the subsequent investigations.

Figure 3 shows ADF-STEM and bright-field STEM images of Rh-deposited Ta_3N_5/$KTaO_3$, in which rhodium metal was photodeposited on Ta_3N_5/$KTaO_3$ nitrided for 0.25 h from $RhCl_3$ using methanol as a hole scavenger. Small rhodium metal clusters were predominantly formed on the surfaces of the Ta_3N_5 nanorods rather than on the $KTaO_3$ crystals. SEM images (Supplementary Fig. 7a,b) also confirm the selective photodeposition of rhodium metal clusters on the Ta_3N_5/$KTaO_3$ following a 4 h nitridation process. Because Rh^{3+} ions are reduced by photoexcited electrons during the photodeposition process[29], the location of the rhodium clusters is evidently associated with reduction sites for hydrogen evolution during water splitting. Similarly, the oxidative photodeposition of MnO_x from Mn^{2+} ions using $NaIO_3$ as an electron acceptor has been examined in an attempt to determine the location of oxidation sites on the photocatalyst[30]. As shown in the SEM images (Supplementary Fig. 7c,d), flocculent MnO_x was selectively deposited on the Ta_3N_5 nanorods, with little deposition on the $KTaO_3$ cubes. These observations clearly demonstrate that the rod-like Ta_3N_5 single crystals possessed active sites capable of promoting the photocatalytic evolution of both H_2 and O_2 from water under visible light.

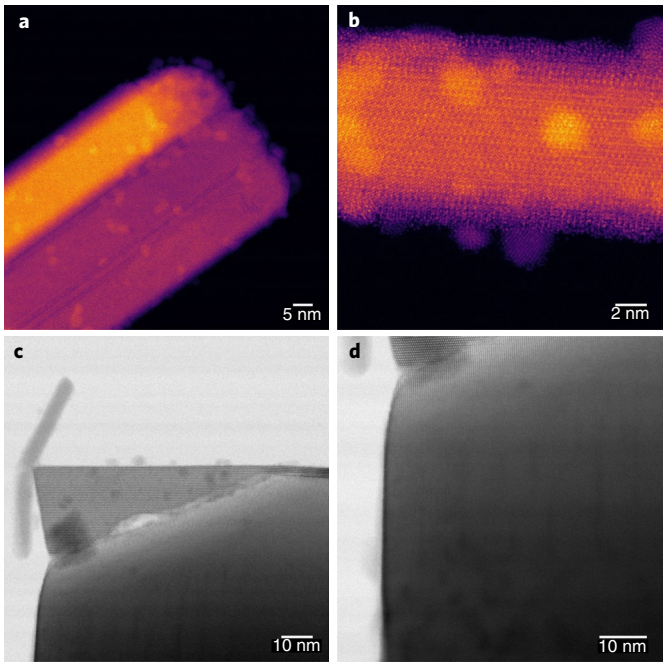

Fig. 3 | Selective photodeposition of rhodium metal particles on Ta_3N_5 nanorods. a–d, ADF-STEM (**a** and **b**) and bright-field STEM (**c** and **d**) images of 0.02 wt% Rh-modified Ta_3N_5/$KTaO_3$ synthesized with a nitridation time of 0.25 h.

Because the mass fraction of Ta_3N_5 in the Ta_3N_5/$KTaO_3$ varied with nitridation time (Fig. 1, Supplementary Fig. 2 and Supplementary Table 2), the effects of the nitridation time and the Rh/Cr_2O_3 co-catalyst loading were investigated in detail. Figure 4a plots the photocatalytic activity of the Ta_3N_5/$KTaO_3$ as a function of the nitridation time, while the gas evolution rates over the respective photocatalysts as functions of time are presented in Supplementary Fig. 8. The activity evidently increased sharply with increasing nitridation time, reaching a maximum at 0.25 h and then dramatically decreasing with further nitridation. The ratios of the amounts of H_2 and O_2 evolved were close to the stoichiometric ratio expected from the decomposition of H_2O into H_2 and O_2. Figure 4b and Supplementary Fig. 9 show the correlation between the photocatalytic activity and the amount of rhodium loaded on Ta_3N_5/$KTaO_3$ specimens prepared using 0.25, 0.5 and 4 h nitridation processes. As the nitridation time decreased, the maximum photocatalytic activity appeared at lower rhodium loadings, indicating that the optimum rhodium content is correlated with the mass fraction of Ta_3N_5 in the Ta_3N_5/$KTaO_3$. The maximum H_2 and O_2 evolution rates were obtained for the Ta_3N_5/$KTaO_3$ prepared using a 0.25 h nitridation process, which had a low density of Ta_3N_5 nanorods (1.4 wt% of the total Ta_3N_5/$KTaO_3$ mass) and a relatively low rhodium co-catalyst loading (0.02 wt% of the total Ta_3N_5/$KTaO_3$ mass). These results provide further evidence that the Ta_3N_5 nanorods represent the active sites for overall water splitting on Ta_3N_5/$KTaO_3$. The evident increase in the activity with increasing nitridation time from 0.05 to 0.25 h is attributed to the increase in the density of the Ta_3N_5 nanorod crystals. However, the Ta_3N_5/$KTaO_3$ samples that were nitrided for longer durations beyond 0.25 h benefited to a greater extent from heavier loading of the Rh/Cr_2O_3 co-catalyst, while exhibiting lower activities. These effects are believed to be due to deterioration of the quality of the Ta_3N_5 nanorods during prolonged exposure to NH_3 at high temperature. As described, the disordered surface atoms (Fig. 2i) and increased background absorption in the UV-Vis DRS (Fig. 1c) suggest the formation of structural defects in Ta_3N_5 nanorod crystals

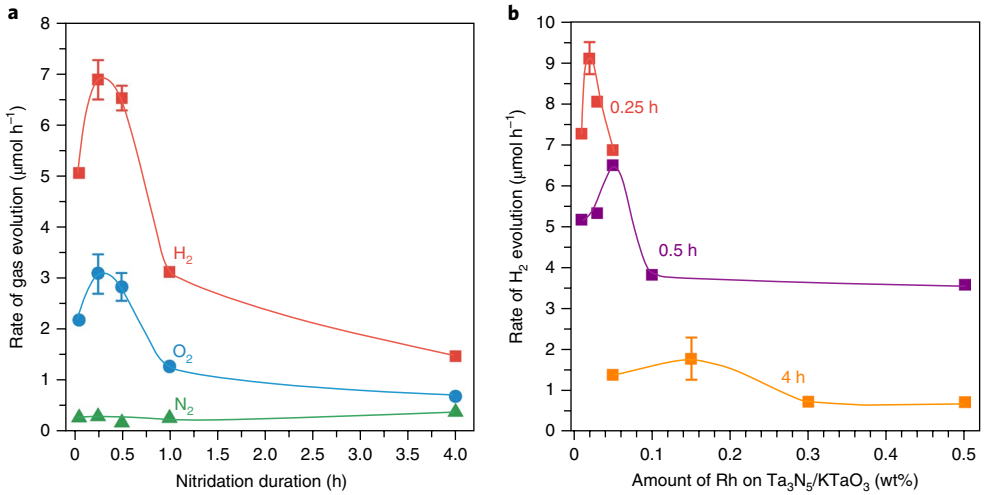

Fig. 4 | Effect of the nitridation time and co-catalyst loading amount on the overall-water-splitting activity of Rh/Cr_2O_3-modified Ta_3N_5/$KTaO_3$. a, Gas evolution rates during overall water splitting as functions of the Ta_3N_5/$KTaO_3$ nitridation time, with 0.05 wt% rhodium loading on Ta_3N_5/$KTaO_3$. **b**, H_2 evolution rates as functions of the rhodium loading during overall water splitting over Rh/Cr_2O_3-modified Ta_3N_5/$KTaO_3$ synthesized with nitridation times of 0.25, 0.5 and 4 h. The error bars show s.d. Conditions: 0.15 g catalyst; 150 ml ultrapure water; 300 W xenon lamp ($\lambda \geq 420$ nm) light source.

during the long-time nitridation. Such surface defect states generated by the prolonged exposure to NH_3 at high temperature can act as recombination and trapping centres for photoexcited charges[20,27], which is detrimental to the photocatalytic performance of Ta_3N_5 nanorods. Moreover, the increase in the size of Ta_3N_5 nanorods with nitridation time leads to a long migration pathway for the excited charge carriers and thus raises the charges recombination probability[31,32]. It is worth noting that the oxygen contents of Ta_3N_5 nanorods in the Ta_3N_5/$KTaO_3$ nitrided for 0.25 and 4 h were similar (see Supplementary Fig. 10 and the accompanying discussion). This indicates that the oxygen impurity is not responsible for the difference in photocatalytic activity. Thus, the absence of defect states in the Ta_3N_5 nanorod single crystals through a brief nitridation process allows the efficient migration of photogenerated charges towards the surface sites, which in turn enables the one-step-excitation overall-water-splitting reaction. In comparison, Ta_3N_5/$LiTaO_3$ and Ta_3N_5/$NaTaO_3$, in which the Ta_3N_5 components were polycrystalline aggregates, exhibited negligible photocatalytic activities (Supplementary Fig. 11). In addition, Ta_3N_5, having a high defect density and polycrystalline particles prepared from Ta_2O_5 by the conventional severe nitridation process, failed to split water photocatalytically (Supplementary Fig. 11). Therefore, the single-crystal nanorod is an ideal architecture capable of enhancing the transfer and collection of photoexcited charges in the Ta_3N_5 semiconductor[23,33].

The stability of the photocatalytic activity was examined using a Ta_3N_5/$KTaO_3$ photocatalyst prepared using the optimal nitridation time, Rh/Cr_2O_3 loading and photocatalyst amount dispersed in water (Supplementary Fig. 12). Figure 5a presents H_2 and O_2 evolutions acquired during a typical overall-water-splitting trial under visible light ($\lambda \geq 420$ nm). Both H_2 and O_2 were evolved simultaneously, at a near-stoichiometric molar ratio of 2:1, while the evolution of N_2 was negligible. The repetition of this reaction using the same sample after evacuating the gas phase resulted in essentially the same evolution of H_2 and O_2, demonstrating the stability of Rh/Cr_2O_3-loaded Ta_3N_5/$KTaO_3$ during the decomposition of water under visible-light irradiation. The photocatalyst also exhibited stability under simulated sunlight (Fig. 5b). The STH energy conversion efficiency of this material was estimated to be 0.014%. The apparent quantum efficiency (AQE) values for the photocatalyst during overall water splitting as a function of the irradiation wavelength are presented in Fig. 5c. The AQE values were 2.2% at 320 nm (±25 nm), 0.22% at 420 nm (±25 nm) and 0.024% at 500 nm (±25 nm). The large increase in the AQE at wavelengths shorter than 350 nm is attributed to the excitation of the $KTaO_3$ by ultraviolet irradiation. Interestingly, the AQE became markedly lower compared with the absorption profile at wavelengths longer than 440 nm even though the photocatalyst was observed to split water under visible light up to 560 nm. This effect is probably associated with the low absorption coefficient for Ta_3N_5 in the visible-light region beyond 500 nm[27,34,35].

We have previously reported a number of visible-light-driven particulate tantalum-based oxynitride photocatalysts that are active in one-step-excitation water splitting, such as TaON (band gap energy, $E_g = 2.5$ eV)[36], $CaTaO_2N$ ($E_g = 2.4$ eV)[36] and $LaMg_xTa_{1-x}O_{1+3x}N_{2-3x}$ ($E_g = 2.1$ eV)[11], all of which have d^0 electronic configurations. The rod-like single-crystal Ta_3N_5 prepared by the brief nitridation of $KTaO_3$ in the present work shows higher visible-light activity than the above photocatalysts because structural defects, such as surface defect states and grain boundaries, are absent. However, the total efficiency of Ta_3N_5/$KTaO_3$ for overall water splitting is still lower than that of $(Ga_{1-x}Zn_x)(N_{1-x}O_x)$ ($E_g = 2.6$ eV)[10] and $(Zn_{1+x}Ge)(N_2O_x)$ ($E_g = 2.7$ eV)[36], both of which have d^{10} electronic configurations, despite its longer absorption edge wavelength. This might be due to the sparse distribution of nanorod Ta_3N_5 single crystals in the Ta_3N_5/$KTaO_3$, in which each Ta_3N_5 nanorod is located at one edge of cubic $KTaO_3$, such that much of the incident light can pass through and is scattered without being absorbed by the Ta_3N_5. Thus, it is possible that the photocatalyst performance could be considerably improved by increasing the relative proportion of such high-quality Ta_3N_5 nanorod single crystals in the Ta_3N_5/$KTaO_3$. Efforts to improve the surface area of $KTaO_3$ by reducing the particle size and selectively exposing more $KTaO_3$ (110) faces that are the growth sites for Ta_3N_5 nanorods are ongoing to increase the density of highly crystalline Ta_3N_5 nanorods. Another aspect worthy of consideration is the high oxygen density in Ta_3N_5 nanorods on $KTaO_3$ (Supplementary Fig. 10). It has been suggested that certain kinds of oxygen impurities do not deteriorate the quality of Ta_3N_5, but enhance the structural stability and photocatalytic/photoelectrochemical performance of Ta_3N_5 material[37,38]. However, it is still an open question whether this is applicable to Ta_3N_5 photocatalysts used for the overall-water-splitting reaction. Doping

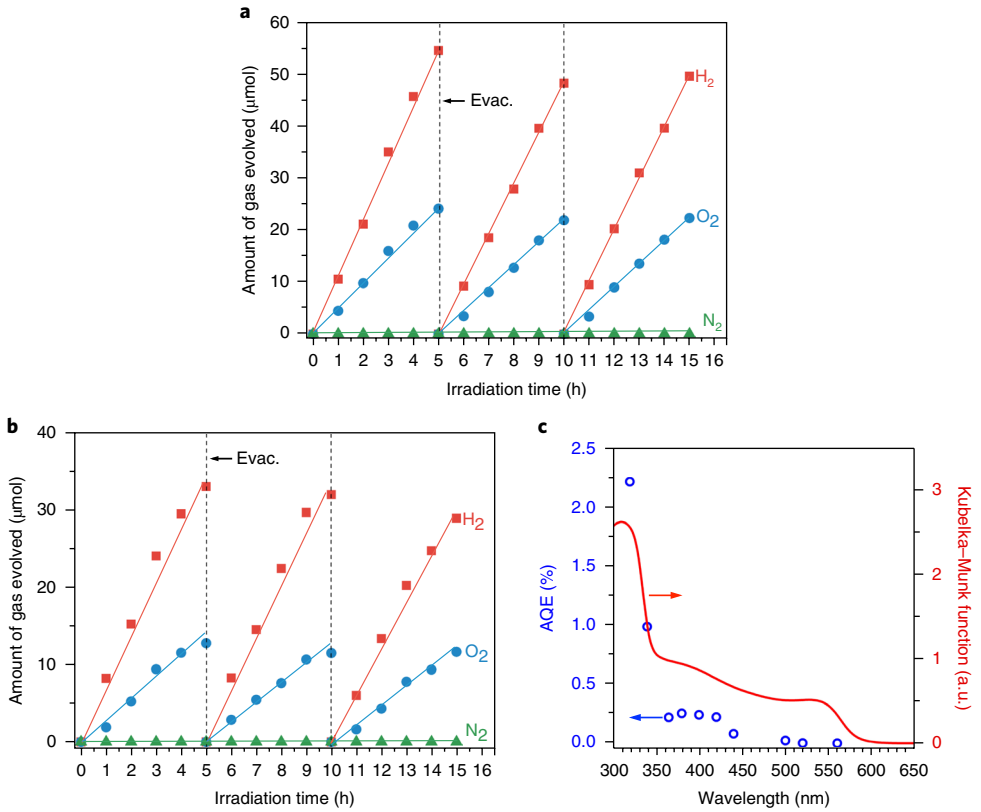

Fig. 5 | Overall-water-splitting performance and AQE of Rh/Cr_2O_3-modified Ta_3N_5/$KTaO_3$. a,**b**, Time courses of gas evolution during overall water splitting over Rh/Cr_2O_3-modified Ta_3N_5/$KTaO_3$ synthesized with a nitridation time of 0.25 h under visible light ($\lambda \geq 420$ nm) (**a**) and simulated sunlight (**b**). The dashed lines represent the points when the overall-water-splitting reaction restarts after the removal of gas products by evacuation (evac.). **c**, AQE as a function of the incident light wavelength in overall water splitting over Rh/Cr_2O_3-modified Ta_3N_5/$KTaO_3$ synthesized with a nitridation time of 0.25 h. Conditions: 0.3 g catalyst; 0.02 wt% rhodium loading; 150 ml ultrapure water; 300 W xenon lamp ($\lambda \geq 420$ nm) light source or solar simulator (AM 1.5 G). For the measurement of AQE, the 300 W xenon lamp was equipped with various band-pass filters.

of lower-valent cations will be worthy of investigation because it allows Ta_3N_5 to accommodate oxygen anions to maintain the charge neutrality and potentially enhance the efficiency of Ta_3N_5 nanorod single crystals.

Conclusions

In summary, the formation of well-defined Ta_3N_5 nanorod single crystals on $KTaO_3$ by brief NH_3 nitridation, without grain boundaries and surface defect states, afforded a photocatalyst that was active for overall water splitting under visible-light irradiation when modified with a core-shell-structured Rh/Cr_2O_3 co-catalyst. The volatilization of potassium species from the lattice-matched surface of $KTaO_3$ during the nitridation controls the substitution of nitrogen for oxygen and facilitates the evolution of discrete Ta_3N_5 nanorod single crystals free from grain boundaries. Moreover, the brief exposure of Ta_3N_5 to the reducing NH_3 atmosphere effectively minimizes the formation of defects in the Ta_3N_5 single crystals. Accordingly, such Ta_3N_5 nanorod single crystals enable the photoexcited charges to transfer expeditiously from the interior of the nanoscaled structure to the surface. Although the present efficiency is still low, the findings clearly demonstrate the achievement of one-step-excitation overall water splitting after refinement of the photocatalyst to suppress the undesirable defects in the structure. The strategy of choosing appropriate precursors with matching lattice parameters and volatile components is expected to enable the fabrication of more efficient nanoscale single-crystal photocatalysts and contribute to the development of solar energy conversion.

Methods

Synthesis of Ta_3N_5 nanorod single crystals on $KTaO_3$ particles. $KTaO_3$ particles were fabricated by a conventional solid-state reaction method[39]. Ta_2O_5 (99.9%; Kojundo Chemical Laboratory) and K_2CO_3 (99.5%; Kanto Chemical) were mixed at a Ta:K molar ratio of 1:1.05. Excess potassium was added to compensate for losses by volatilization at high temperatures. The mixture was thoroughly ground in an agate mortar for 90 min in the presence of a small amount of ethanol as a dispersant. After drying, the resulting mixture was transferred into an alumina crucible and calcined at 1,173 K for 1 h and then at 1,423 K for 10 h in static air. The $KTaO_3$ obtained in this manner was washed with ultrapure water at 343 K for 2 h and centrifuged twice to remove any residual K_2CO_3. The powder was then completely dried by heating at 343 K overnight. Subsequently, the as-prepared $KTaO_3$ was subjected to a nitridation process to obtain Ta_3N_5 grown on $KTaO_3$. $KTaO_3$ (0.5 g) was transferred into an alumina tube and nitrided at 1,173 K for time spans ranging from 0.05 to 4 h under a flow of gaseous NH_3 at 100 ml min^{-1}. Samples of Ta_3N_5 on $LiTaO_3$ or $NaTaO_3$ were synthesized using the same procedure, but with Li_2CO_3 (99.95%; Kanto Chemical) or Na_2CO_3 (99.8%; Wako Pure Chemical Industries) in place of the K_2CO_3, respectively. For comparison, $KTaO_3$ was also nitrided under the same conditions, but with an additional 5 mol% K_2CO_3.

Photodeposition of a metal-Cr_2O_3 core-shell co-catalyst or MnO_x on Ta_3N_5/$KTaO_3$ photocatalysts. A metal-Cr_2O_3 core-shell co-catalyst for H_2 evolution was loaded on Ta_3N_5/$KTaO_3$ photocatalysts by a previously reported two-step photodeposition process[40]. A metal core was first photodeposited on the Ta_3N_5/$KTaO_3$ photocatalyst, using $RhCl_3{\cdot}3H_2O$ (Kanto Chemical), $H_2PtCl_6{\cdot}6H_2O$ (> 98.5%; Kanto Chemical), $Na_2IrCl_6{\cdot}6H_2O$ (>97.0%; Kanto Chemical) or $RuCl_3{\cdot}3H_2O$ (>98.0%; Kanto Chemical) as the metal precursor. This was accomplished by dispersing Ta_3N_5/$KTaO_3$ powder in 150 ml of an aqueous methanol solution (10 vol%) containing the required amount of the metal precursor. The pH of this solution was not adjusted, but the temperature was maintained at 288 K by circulating cooling water. The suspension was evacuated to completely remove

dissolved air and then exposed to visible light ($\lambda \geq 420$ nm) with continuous stirring. The photodeposition time was varied from 3 to 12 h depending on the metal precursor and loading amount. Typically, the photodeposition of rhodium was conducted over 3 h. In the second step, a Cr_2O_3 shell was formed on the surface of the metal core, using the photoreduction of Cr^{6+} to suppress backward reactions. The mass ratio between the Cr_2O_3 shell and the metal core was held constant at 3:1. K_2CrO_4 (99.0%; Kanto Chemical) was added to the above solution as a Cr^{6+} precursor without pH adjustment. After complete degassing, the suspension was irradiated with ultraviolet light ($\lambda \geq 300$ nm) because the reduction of Cr^{6+} progressed very slowly under visible light ($\lambda \geq 420$ nm). After 12 h of irradiation, the photocatalyst was removed by filtering, washed three times with ultrapure water and dried at 313 K under vacuum.

MnO_x was photodeposited on the $Ta_3N_5/KTaO_3$ photocatalyst by mixing $Ta_3N_5/KTaO_3$ powder and $Mn(NO_3)_2{\cdot}6H_2O$ (98.0%; Sigma–Aldrich) as the precursor in an aqueous solution (150 ml) containing 0.2 M $NaIO_3$ as an electron acceptor. After irradiation with visible light ($\lambda \geq 420$ nm) for 12 h, the powder was removed by filtering, washed and dried before characterization.

Characterizations of material. SEM images were obtained using a Hitachi SU8020 system. Angle ADF-STEM and energy-dispersive X-ray spectroscopy (EDS) were conducted with ARM200F microscopes and a JED-2300T EDS system. XRD patterns were acquired using a Rigaku Ultima III with Cu Kα radiation, operating at 40 kV and 40 mA. UV-Vis DRS was conducted using a spectrometer (V-570; Jasco).

Overall-water-splitting reaction. Photocatalytic reactions were carried out in a Pyrex top-illuminated reaction vessel connected to a closed gas-circulation system. A photocatalyst loaded with a metal/Cr_2O_3 core-shell co-catalyst was dispersed in ultrapure water (150 ml) to give a pH of approximately 7. After completely removing air from the reaction slurry by evacuation, the suspension was irradiated with a 300 W xenon lamp equipped with a cold mirror and a cut-off filter (L42, $\lambda \geq 420$ nm) or a solar simulator (SAN-EI electronic, XES40S1, AM 1.5 G, 100 mW cm^{-2}). The reactant solution was maintained at 288 K by a cooling water system during the reaction. The evolved gas products were analysed using an online thermal-conductivity-detector gas chromatography system consisting of a GC-8A chromatograph (Shimadzu) equipped with a molecular sieve 5 Å column, with argon as the carrier gas.

STH conversion efficiency measurements. The water-splitting reaction was performed under simulated solar irradiation. The STH conversion efficiency is given by

$$\mathrm{STH}(\%) = (R(\mathrm{H_2}) \times \Delta G_r) / (P \times S) \times 100$$

where $R(H_2)$, ΔG_r, P and S denote the rate of hydrogen evolution during the overall-water-splitting reaction, the Gibbs energy for the reaction $H_2O(l) \rightarrow H_2(g) + 1/2O_2(g)$, the energy intensity of the AM 1.5 G solar irradiation (100 mW cm^{-2}) and the irradiated sample area (38.2 cm^2), respectively. The value of ΔG_r used for the calculations was 237 kJ mol^{-1} at 288 K.

AQE measurement. The AQE for overall water splitting based on one-step photoexcitation is given by

$$\mathrm{AQE}(\%) = [2 \times n(\mathrm{H_2})] / n(\mathrm{photons}) \times 100,$$

where $n(H_2)$ and n(photons) represent the number of H_2 molecules generated and the number of incident photons, respectively. The overall-water-splitting reaction and measurement of the number of incident photons were carried out using the same light source equipped with various band-pass filters.

Data availability. The data that support the findings of this study are available from the corresponding author upon reasonable request.

Received: 5 May 2018; Accepted: 26 July 2018;
Published online: 3 September 2018

References

1. Lewis, N. S. Toward cost-effective solar energy use. *Science* **315**, 798–801 (2007).
2. Chen, X., Shen, S., Guo, L. & Mao, S. Semiconductor-based photocatalytic hydrogen generation. *Chem. Rev.* **110**, 6503–6570 (2010).
3. Hisatomi, T., Kubota, J. & Domen, K. Recent advances in semiconductors for photocatalytic and photoelectrochemical water splitting. *Chem. Soc. Rev.* **43**, 7520–7535 (2014).
4. Wang, Q. et al. Scalable water splitting on particulate photocatalyst sheets with a solar-to-hydrogen energy conversion efficiency exceeding 1%. *Nat. Mater.* **15**, 611–615 (2016).
5. Grätzel, M. Photoelectrochemical cells. *Nature* **414**, 338–344 (2001).
6. Verlage, E. et al. A monolithically integrated, intrinsically safe, 10% efficient, solar-driven water-splitting system based on active, stable earth-abundant electrocatalysts in conjunction with tandem III–V light absorbers protected by amorphous TiO_2 films. *Energy Environ. Sci.* **8**, 3166–3172 (2015).
7. May, M. M., Lewerenz, H. J., Lackner, D., Dimroth, F. & Hannappel, T. Efficient direct solar-to-hydrogen conversion by in situ interface transformation of a tandem structure. *Nat. Commun.* **6**, 8286 (2015).
8. Pinaud, B. A. et al. Technical and economic feasibility of centralized facilities for solar hydrogen production via photocatalysis and photoelectrochemistry. *Energy Environ. Sci.* **6**, 1983–2002 (2013).
9. Fabian, D. M. et al. Particle suspension reactors and materials for solar-driven water splitting. *Energy Environ. Sci.* **8**, 2825–2850 (2015).
10. Maeda, K. et al. Photocatalyst releasing hydrogen from water. *Nature* **440**, 295 (2006).
11. Pan, C. et al. A complex perovskite-type oxynitride: the first photocatalyst for water splitting operable at up to 600 nm. *Angew. Chem. Int. Ed.* **54**, 2955–2959 (2015).
12. Goto, Y. et al. A particulate photocatalyst water-splitting panel for large-scale solar hydrogen generation. *Joule* **2**, 509–520 (2018).
13. Chiang, T. et al. Efficient photocatalytic water splitting using Al-doped $SrTiO_3$ coloaded with molybdenum oxide and rhodium-chromium oxide. *ACS Catal.* **8**, 2782–2788 (2018).
14. Kudo, A. & Miseki, Y. Heterogeneous photocatalyst materials for water splitting. *Chem. Soc. Rev.* **38**, 253–278 (2009).
15. Zhang, G., Lan, Z., Lin, L., Lin, S. & Wang, X. Overall water splitting by Pt/g-C_3N_4 photocatalysts without using sacrificial agents. *Chem. Sci.* **7**, 3062–3065 (2016).
16. Jo, W. J. et al. Phase transition-induced band edge engineering of $BiVO_4$ to split pure water under visible light. *Proc. Natl Acad. Sci. USA* **112**, 13774–13778 (2015).
17. Tanaka, A., Teramura, K., Hosokawa, S., Kominami, H. & Tanaka, T. Visible light-induced water splitting in an aqueous suspension of a plasmonic Au/TiO_2 photocatalyst with metal co-catalysts. *Chem. Sci.* **8**, 2574–2580 (2017).
18. Hitoki, G. et al. Ta_3N_5 as a novel visible light-driven photocatalyst ($\lambda < 600$ nm). *Chem. Lett.* **31**, 736–737 (2002).
19. Ma, S., Hisatomi, T., Maeda, K., Moriya, Y. & Domen, K. Enhanced water oxidation on Ta_3N_5 photocatalysts by modification with alkaline metal salts. *J. Am. Chem. Soc.* **134**, 19993–19996 (2012).
20. Chen, S. et al. Interface engineering of a CoO_x/Ta_3N_5 photocatalyst for unprecedented water oxidation performance under visible-light-irradiation. *Angew. Chem. Int. Ed.* **54**, 3047–3051 (2015).
21. Hou, J. et al. In situ phase-induced spatial charge separation in core–shell oxynitride nanocube heterojunctions realizing robust solar water splitting. *Adv. Energy Mater.* **7**, 1700171 (2017).
22. Qi, Y. et al. Achievement of visible-light-driven Z-scheme overall water splitting using barium-modified Ta_3N_5 as a H_2-evolving photocatalyst. *Chem. Sci.* **8**, 437–443 (2017).
23. Li, Y. et al. Cobalt phosphate-modified barium-doped tantalum nitride nanorod photoanode with 1.5% solar energy conversion efficiency. *Nat. Commun.* **4**, 2566 (2013).
24. Li, M. et al. A cocatalyst-loaded Ta_3N_5 photoanode with a high solar photocurrent for water splitting upon facile removal of the surface layer. *Angew. Chem. Int. Ed.* **52**, 1–6 (2013).
25. Liu, G. et al. Enabling an integrated tantalum nitride photoanode to approach the theoretical photocurrent limit for solar water splitting. *Energy Environ. Sci.* **9**, 1327–1334 (2016).
26. Zhong, M. et al. Highly active GaN-stabilized Ta_3N_5 thin-film photoanode for solar water oxidation. *Angew. Chem. Int. Ed.* **56**, 4739–4743 (2017).
27. Nurlaela, E., Ziani, A. & Takanabe, K. Tantalum nitride for photocatalytic water splitting: concept and applications. *Mater. Renew. Sustain. Energy* **5**, 18 (2016).
28. Maeda, K. et al. Noble-metal/Cr_2O_3 core/shell nanoparticles as a cocatalyst for photocatalytic overall water splitting. *Angew. Chem. Int. Ed.* **45**, 7806–7809 (2006).
29. Teramura, K. et al. In situ time-resolved energy-dispersive XAFS study on photodeposition of Rh particles on a TiO_2 photocatalyst. *J. Phys. Chem. C* **112**, 8495–8498 (2008).
30. Li, R. et al. Spatial separation of photogenerated electrons and holes among {010} and {110} crystal facets of $BiVO_4$. *Nat. Commun.* **4**, 1432 (2013).
31. Chen, X., Li, C., Grätzel, M., Kosteckid, R. & Mao, S. S. Nanomaterials for renewable energy production and storage. *Chem. Soc. Rev.* **41**, 7909–7937 (2012).
32. Osterloh, F. E. Inorganic nanostructures for photoelectrochemical and photocatalytic water splitting. *Chem. Soc. Rev.* **42**, 2294–2320 (2013).
33. Wang, L. et al. Tantalum nitride nanorod arrays: introducing Ni–Fe layered double hydroxides as a cocatalyst strongly stabilizing photoanodes in water splitting. *Chem. Mater.* **27**, 2360–2366 (2015).

34. Pinaud, B. A., Vesborg, P. C. K. & Jaramillo, T. F. Effect of film morphology and thickness on charge transport in Ta_3N_5/Ta photoanodes for solar water splitting. *J. Phys. Chem. C* **116**, 15918–15924 (2012).
35. Hajibabaei, H., Zandi, O. & Hamann, T. W. Tantalum nitride films integrated with transparent conductive oxide substrates via atomic layer deposition for photoelectrochemical water splitting. *Chem. Sci.* **7**, 6760–6767 (2016).
36. Chen, S., Takata, T. & Domen, K. Particulate photocatalysts for overall water splitting. *Nat. Rev. Mater.* **2**, 17050 (2017).
37. Wang, J., Feng, J., Zhang, L., Li, Z. & Zou, Z. Role of oxygen impurity on the mechanical stability and atomic cohesion of Ta_3N_5 semiconductor photocatalyst. *Phys. Chem. Chem. Phys.* **16**, 15375–15380 (2014).
38. Xie, Y., Wang, Y., Chen, Z. & Xu, X. Role of oxygen defects on the photocatalytic properties of Mg-doped mesoporous Ta_3N_5. *ChemSusChem* **9**, 1403–1412 (2016).
39. Kato, H. & Kudo, A. Water splitting into H_2 and O_2 on alkali tantalate photocatalysts $ATaO_3$ (A = Li, Na, and K). *J. Phys. Chem. B* **105**, 4285–4292 (2001).
40. Maeda, K. et al. Preparation of core-shell-structured nanoparticles (with a noble-metal or metal oxide core and a chromia shell) and their application in water splitting by means of visible light. *Chem. Eur. J.* **16**, 7750–7759 (2010).
41. Momma, K., & Izumi, F. VESTA 3 for three-dimensional visualization of crystal, volumetric and morphology data. *J. Appl. Crystallogr.* **44**, 1272–1276 (2011).

Acknowledgements

This work was financially supported by the Artificial Photosynthesis Project of the New Energy and Industrial Technology Development Organization and Grants-in-Aid for Scientific Research (A) (number 16H02417), Scientific Research (C) (number 16K06862) and Young Scientists (A) (number 15H05494) from the Japan Society for the Promotion of Science.

Author contributions

Z.W., Y.Inoue and K.D. conceived the material growth design. Z.W. fabricated the photocatalyst materials, and conducted the XRD, UV-Vis DRS and SEM characterizations, co-catalyst modifications and overall-water-splitting reactions. R.I., N.S. and Y.Ikuhara carried out the ADF-STEM and STEM-EDS measurements. Q.W. conducted the AQE and STH measurements. Y.Inoue, T.H., T.T. and K.D. supervised the research work. Z.W., Y.Inoue, T.H., Q.W., T.T., S.C. and K.D. contributed to valuable discussion. Z.W., Y.Inoue, T.H. and K.D. wrote and revised the paper. All authors commented on the paper.

Competing interests

The authors declare no competing interests.

Additional information

Supplementary information is available for this paper at https://doi.org/10.1038/s41929-018-0134-1.

Reprints and permissions information is available at www.nature.com/reprints.

Correspondence and requests for materials should be addressed to K.D.

Publisher's note: Springer Nature remains neutral with regard to jurisdictional claims in published maps and institutional affiliations.